Journal of Nuclear Materials 616 (2025) 156091

Contents lists available at ScienceDirect

Journal of Nuclear Materials

journal homepage: www.elsevier.com/locate/jnucmat

# Characterization of $He^+$ implanted W-Zr-B thin films deposited by HiPIMS on additively manufactured Inconel 617 as a candidate system for nuclear components

Józef Rzempołuch [a], Tomasz Stasiak [a], Marcin Maździarz [b], Jarosław Jasiński [a,d], Udisien Woy [c], Rafał Psiuk [b], Marcin Kowal [a], Anna Kosińska [d], Magdalena Wilczopolska [d], Katarzyna Mulewska [a,d], Marek Barlak [e], Katarzyna Ciporska [a], Łukasz Kurpaska [a,d], Jacek Jagielski [a,d,e], Tomasz Mościcki [b,*]

[a] Materials Research Laboratory, National Centre for Nuclear Research, Otwock, Poland
[b] Institute of Fundamental Technological Research, Polish Academy of Sciences, Warsaw, Poland
[c] University of Sheffield, Nuclear Advanced Manufacturing Research Centre, Brunel Way, Rotherham, United Kingdom
[d] NOMATEN Centre of Excellence, National Centre for Nuclear Research, Otwock, Poland
[e] Material Physics Department, National Centre for Nuclear Research, Otwock, Poland

## HIGHLIGHTS

- Hard DFT-designed W-Zr-B coatings deposited using HiPIMS on AM Inconel 617.
- High mechanical properties and good adhesion of films to metallic substrate.
- Amorphous character of the deposited W-Zr-B thin films confirmed by TEM observations.
- Helium swelling effect during ion implantation caused a hardness decrease.
- Smaller decrease in mechanical properties after irradiation at 400 °C than at RT.

## GRAPHICAL ABSTRACT

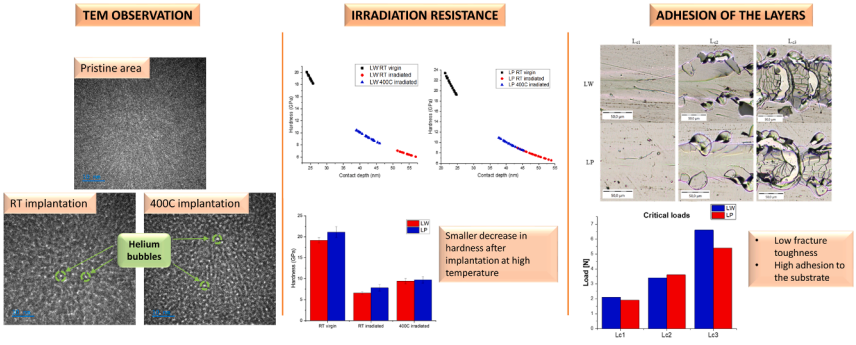


## ARTICLE INFO

*Keywords:*
Tungsten borides
Hard thin films
High-power impulse magnetron sputtering
$He^+$ ion implantation
Nanoindentation

## ABSTRACT

Tungsten boride alloyed with zirconium is considered a very promising material in the nuclear industry due to its shielding properties. In this paper, the resistance to helium irradiation of W-Zr-B thin films deposited on additively manufactured Inconel 617 is investigated. Two laser Directed Energy Deposition methods, a laser powder (DED-LP) and laser wire (DED-LW) were utilized for Inconel 617 substrate preparation. Preliminary studies with density functional theory (DFT) calculations were performed to determine the stability and theoretical values of structural and mechanical properties of fabricated coatings. Additionally to structural and mechanical properties, an irradiation effects after ion implantation of the layers at room temperature and 400 °C with $He^+$ ion dose of 5 $\times$ $10^{17}$ ions/cm$^2$ and energy of 60 keV were also studied. The results show that HiPIMS is a reliable process that allows depositing dense and uniform coatings with excellent mechanical properties, comparable with DFT

* Corresponding author.
*E-mail address:* tmosc@ippt.pan.pl (T. Mościcki).

https://doi.org/10.1016/j.jnucmat.2025.156091
Received 27 February 2025; Received in revised form 26 June 2025; Accepted 4 August 2025
Available online 6 August 2025

calculations. Scratch test results confirmed good adhesion to the surface regardless of the substrate despite low critical forces values (5.4 N and 6.6 N $L_{c3}$ values). The thickness of the deposited coatings varied from 2.40 to 2.50 μm. Nevertheless, after helium ion implantation, TEM observation shows helium voids and bubbles form at the near-surface area of the coatings. A significant decrease in hardness from initial 21.12 GPa to 6.51 GPa (LW), 7.83 GPa (LP) after room temperature and 9.40 GPa (LW), 9.71 GPa (LP) after 400 °C ion implantation, respectively is observed. The mechanism underlying this effect is also discussed in the article.

## 1. Introduction

As global warming and global energy deficit are becoming significant concerns, more efficient and environment-friendly ways to produce energy are required. Generation IV nuclear reactors appear to be a promising solution to the mentioned problems. However, construction materials building those reactors are exposed to extreme conditions, such as a highly corrosive environment, extremely high temperatures, and radiation. Therefore, there is a constant need to develop novel materials that can withstand this highly hostile environment. Due to the high operating temperature parameters of the new generation plants, in the range of more than 650 to even 1000 °C, the selection of materials comes down to only a few structural materials. Materials that are taken into account as structural elements and meet stringent design requirements are nickel alloys, and among these alloys is Inconel 617. Inconel 617 is a nickel-based, austenitic, solid solution-strengthened superalloy. Due to its exceptional properties, creep resistance, and high-temperature mechanical properties, alloy 617 is applicable in various industries such as aerospace, power plants, and the chemical industry [1]. Moreover, thanks to its chemical composition (presence of chromium, molybdenum, and aluminium), Inconel 617 exhibits excellent corrosion resistance in various corrosive environments [2]. In addition, this alloy was qualified in 2020 by the American Society of Mechanical Engineers (ASME) for nuclear applications with the ability to operate at temperatures as high as 950 °C, which, as a result, can be a solution in material concepts used in new reactors [3]. However, the use of Inconel 617 also brings with it the requirements of alternative production routes for these materials, including innovative casting processes and additive manufacturing [4,5]. These last-mentioned production techniques have the potential to support the realization of next-generation reactors designs while solving persistent problems, including costly and long-lasting repairs and related manufacturing requirements, etc., thus posing a new research challenge in evaluating their properties for different components, operation conditions and resistance to high dose radiation. Helium-induced damage is a significant threat to materials exposed to a working reactor environment since it is produced as a result of the (n, α) transmutation reaction [6]. Helium irradiation leads to the formation of helium bubbles, swelling, and helium-induced embrittlement, leading to a dramatic decrease in the mechanical properties of materials [7]. Despite the unique properties mentioned, Inconel 617, irradiation resistance is one of the biggest challenges for alloy 617 application in generation IV reactors. Zhu et al. analysed the irradiation resistance of Hastelloy N and Inconel 617, when exposed to helium ions [8]. TEM and nanohardness investigations revealed that Alloy 617 exhibits lesser irradiation resistance compared to Hastelloy N. Zhu et al. irradiated Inconel 617 and GH3535 samples by $Xe^{20+}$ ions to assess and compare their irradiation resistance [9]. Considering the unsatisfying irradiation resistance of Alloy 617, there is a need to develop methods of modifying the properties of Inconel 617 to increase its irradiation resistance. Therefore, developing comprehensive nuclear shielding coatings containing both tungsten and boron elements is beneficial to achieving high radiation shielding efficiency.

Tungsten, due to its enormous density, exhibits excellent shielding properties [10], especially for gamma rays [11]. Nevertheless, the neutron shielding properties of pure tungsten are mediocre. Boron, contrarily, exhibits greater neutron shielding properties. It has been proven that the addition of boron into the tungsten shielding material significantly enhances the shielding properties of such materials [12–14]. Transition metal borides, such as tungsten borides, are promising materials that can be used in nuclear equipment [15,16], thanks to their unique combination of properties that are highly desirable in nuclear applications. Additionally, it has been proven recently that doping tungsten boride with tantalum or niobium can lead to an increase in the hardness of tungsten boride [17,18]. A similar increase in hardness was observed for zirconium doping, which addition significantly improved ductility, fracture resistance and thermal stability at high temperatures (>650 °C), even under thermal shocks [19,20]. Numerous zirconium-doped, tungsten boride coatings were successfully fabricated using spark plasma sintering [20–22], magnetron sputtering [23], and a combination of radio frequency magnetron sputtering and pulsed laser deposition (RFMS-PLD) [24]. Several studies have been conducted to determine the helium irradiation resistance of amorphous materials, stating their good resistance to helium-induced damage [25–27]. For instance, Su et al. analysed the helium irradiation resistance of amorphous silicon oxycarbide. They have proven that amorphous SiOC exhibits relatively good resistance to helium irradiation, and no helium bubbles or volume swelling was observed [28]. They have also demonstrated that in amorphous materials, unlike crystalline, helium remains in solution and is more mobile through atomic-scale diffusion, preventing the formation of defects [29].

In this paper, zirconium-doped tungsten boride coatings were fabricated using High-power Impulse Magnetron Sputtering on additively manufactured Inconel 617. DFT calculations were performed to determine the theoretical values of the coatings' thermal, mechanical and structural properties. Furthermore, deposited coatings were characterized in terms of their microstructure, chemical composition, mechanical properties and adhesion to the substrate. Additionally, the irradiation resistance of coatings was analysed in terms of their application as nuclear radiation shielding materials for generation IV installations.

## 2. Materials and methodology

### 2.1. Density functional theory (DFT) calculations

First-principles calculations were used to define the theoretical values of structural, mechanical and thermal properties of deposited coatings. Density functional theory (DFT) calculations, applying the ABINIT software, were used to optimize the structures ω-type (SG-194, $P6_3/mmc$) and α-type (SG-191, P6/mmm) for $W_{0.875}Zr_{0.125}B_2$ and defected $W_{0.857}Zr_{0.143}B_2$ respectively utilizing and the implemented the pseudopotential plane-wave approximation

(PP-PW). Projector augmented-wave formulation (PAW) pseudopotentials [30] were employed to represent the interactions of the ionic core and non-valence electrons. A local density approximation (LDA) [31] as an exchange-correlation XC functional was chosen. The projector augmented wave method (PAW) pseudopotentials exploit to LDA XC functionals were taken from the PseudoDojo project [32]. The calculation precision settings refer to those presented in [33].

The W-Zr-B targets used for deposition of the protective coatings have the $WB_2$ $P6_3/mmc$ (ω-type) structure [21], which is the most stable and, at the same time, the hardest form of this compound. However, experimental studies show that in magnetron-deposited films, there are defects both in the form of boron and tungsten vacancies, which cause

obtaining the second crystalline form of $WB_2$, i.e. P6/mmm (α-type). Therefore, taking into account the chemical composition of the layers for the purposes of the calculations, 2 × 2 × 2 defected with $WB_2$ cluster (24 – 3 = 21 atoms) supercell of α-type polymorph, and 2 × 2 × 1 (24 atoms) of ω-type $WB_2$ supercell were created. Additionally, one arbitrary tungsten atom was replaced with a zirconium atom. In the structure with defects, a cluster of three atoms was removed, i.e. a triple defect consisting of a W atom and two B atoms; such a defect does not disturb the chemical composition of the metal and the boron. More about the generation and optimization of studied structures and determining formation energy was described in [23].

The theoretical ground state elastic constants $C_{ij}$ of all analysed structures were calculated using the metric tensor formulation of strain in density functional perturbation theory (DFPT) [34]. On the base of a Voigt–Reuss–Hill average [35], the isotropic bulk modulus B, Young's modulus E, shear modulus G and Poisson's ratio $\nu$ were estimated. By calculating Kelvin moduli, i.e. eigenvalues of stiffness tensor written in second-rank tensor notation [36], the mechanical stability of all the structures was examined, where positive definiteness of the stiffness tensor means the stability of structure. Vickers hardness HV and fracture toughness $K_{IC}$ of both modelled samples were estimated using semi-empirical formulas developed in [37].

### 2.2. Substrate characterization

In the experimental part of the study, Inconel 617 was used as a substrate material. Samples were additively manufactured (AM) using Directed Energy Deposition (DED) methods. Two laser DED systems were utilized: a laser powder (DED-LP), comprised of a 15 kW Laserline fibre-coupled diode laser, a gantry-mounted multi-axis robot arm, and a coaxial end-effector for powder deposition, and laser wire (DED-LW) capability, with a 16 kW Trumpf fibre-coupled disk laser, gantry-mounted robot arm, and wire-feeding system. Process parameters are presented in Table 1. The chemical composition of powder and wire feedstock is shown in Table 2. Additively manufactured Inconel 617 samples were cut into 10 × 10 mm pieces.

### 2.3. Deposition of the layers – High power impulse magnetron sputtering (HiPIMS)

Next, W-Zr-B thin films were deposited using the High Power Impulse Magnetron Sputtering (HiPIMS) method from the targets ($W_{1-x}+Zr_x$, where x = 0.16 and metal to B molar ratio of 1/2.5) manufactured using the spark plasma sintering (SPS) technique according to the procedure described in [21]. The target–substrate distance was 80 mm, and the deposition time was 90 min. Before deposition, the surface of Inconel substrates was ground (320-1200 gradation grinding paper), polished (3 μm and 1 μm diamond suspension) and washed in an ultrasonic cleaner in acetone and isopropyl alcohol. Additionally, before deposition, the surface of the substrate was sputtered for 10 min with argon plasma in the vacuum chamber at a pressure of 0.9 Pa. Next, the films were deposited at a pressure of 0.9 Pa (working gas argon) from a two-inch diameter target with a HiPIMS power supply (average input power 250 W, frequency 700 Hz, pulse duration 200 μs, and DC negative potential of 50 V applied to the substrate surface). During deposition, the surface temperature was kept at 400 °C.

**Table 1**
Inconel 617 substrate additive manufacturing DED process parameters.

| *Process parameter* | *DED-LP* | *DED-LW* |
|---|---|---|
| *Power (kW)* | *8* | *10* |
| *Material feed rate* | *83 g/min* | *8 m/min* |
| *Travel speed (mm/min)* | *500* | *800* |
| *Feedstock* | *50–150 μm powder* | *1.2 mm wire* |
| *Layer offset distance (mm)* | *~2* | *~1.6* |

### 2.4. Microstructural characterization

The cross-section and top-view microstructure of the substrates and layers were examined using the HELIOS 5 UX DualBeam scanning electron microscope (SEM), using SEM and STEM modes. The SEM-EDS chemical composition analysis of the layers was conducted using an EDAX Elite Super Detector EDS system with energy in the range of 15 keV. The lamella for transmission electron microscopy (TEM) investigations were prepared using the focused ion beam (FIB) technique using a ThermoFisher Scientific™ Helios™ 5 UX device. The lamella were thinned up to approximately 100 nm. TEM observations of pristine and ion-irradiated layers were performed using a JEOL JEM F200 transmission electron microscope operating at 200 kV. The bright field images and selected area diffraction patterns (SAED) were acquired. To reveal the presence of helium voids, the selected bright field images were taken in the under-focus condition with a defocus of 300 nm. Size and distribution of helium voids were measured using defocused TEM images from the highest peak damage area, according to SRIM calculations and ImageJ software. First, TEM image contrast was enhanced, to highlight the bubbles outline. Next, to reduce noise, the Median filter option with a 2-pixel radius was applied. Finally, helium bubbles were manually outlined and measured.

### 2.5. Adhesion and mechanical testing of W-Zr-B layers

To evaluate the adhesion of the coating, a scratch-test was performed. MCT head was used (Anton Paar) equipped with Rockwell C diamond indenter (radius = 200 μm). Scratch was performed in progressive load mode from 0.03 N to 30 N, scratch length of 4.5 mm and speed of 6 mm/min. During scratch acoustic emission and friction force were recorded. Before and after test scans with a constant load of 0.03 N were performed. Panoramas of scratches were made with an optical microscope at a magnification of 800x.

The mechanical properties of the layers after HiPIMS deposition and after helium ion implantation were evaluated using the nanoindentation technique, employing a NanoTest Vantage System from Micro Materials Ltd. Given the critical influence of tip shape in low-load nanoindentation, the Diamond Area Function (DAF) of the indenter tip was calculated at each indentation depth and incorporated into the analysis [38]. Calibration was conducted with Fused Silica (FS), a material with well-defined mechanical properties, serving as the standard. Experiments were performed at room temperature using a Berkovich-shaped diamond indenter (Synton-MDP) in single-force mode with applied force 1 mN. During the examination, 30 indents were made, with a 20 μm spacing between indents. The loading, unloading, and dwell times were set at 5 s, 2 s, and 3 s, respectively. Nanomechanical properties were extracted from load-displacement curves using the Oliver and Pharr method [39]. To minimize non-irradiated thin film zone influence, the indentation depth was minimized, by choosing very small load.

### 2.6. Helium ion implantation

The ion irradiation/implantation processes were proceeded by the modelling (simulations) of the depth profile of the implanted element and the adequate damage profile, using SRIM-2013.00, the Stopping and Range of Ions in Matter (SRIM) freeware type code (in the mode Detailed Calculation with full Damage Cascades), by James F. Ziegler [40]. Additionally, the following main depth peak parameters: peak volume dopant concentration $N_{max}$, projected range $R_p$, range straggling $\Delta R_p$, skewness, and kurtosis, were determined. The simulation was performed for 100,000 implanted ions of $He^+$, with the energy of 60 keV, perpendicular to the implanted substrate (the ion incidence angle was defined as 0°). In all cases, the simulations were performed for absolute zero. The adopted modelled substrate material W-Zr-B (modelling codes treat the sample as a set of atoms that do not form chemical compounds) had a composition $W_{1-x}Zr_xB_{2.5}$, where x = 0.14 (24.000 at.% of tungsten,

**Table 2**
Chemical composition of AM Inconel 617 substrates.

| Inconel 617 | Element concentration [wt. %] | | | | | | | | | |
|---|---|---|---|---|---|---|---|---|---|---|
| | Ni | Cr | Co | Mo | Al | Fe | | Si | Ti | Mn |
| CRM Material IARM Ni617-18 | 53.30 | 21.90 | 11.81 | 9.33 | 1.08 | 1.45 | 0.21 | | 0.32 | 0.24 |
| LP | 53.23 | 22.99 | 11.66 | 9.34 | 0.98 | 1.94 | 0.10 | | 0.048 | 0.77 |
| LW | 53.91 | 23.21 | 10.69 | 9.30 | 1.13 | 1.66 | 0.04 | | 0.44 | 0.23 |

4.573 at.% of zirconium and 71.430 at.% of boron). The models were compared, and the results were at the same level. The density of the film was 11.258 g/cm$^3$. All the above values were determined for the real material. The displacement per atom (dpa) has been calculated based on the following equation according to the procedure presented by Wyszkowska et al [41].

Thin films were $He^+$ ion-implanted to observe defect behaviour in the layers and evaluate their resistance to the operating conditions in nuclear reactors, compared to the virgin coatings. The ion irradiation processes were provided using a semi-industrial, nonmass-separated implanter of gaseous ions with a continuous ion beam and described in detail elsewhere [42]. Helium of 5 N purity was used as the source of the implanted ions. The implanted fluence was $5 \times 10^{17}$ cm$^{-2}$. The acceleration voltage was 60 kV and therefore, the ion energy was 60 keV, due to the homogeneous ion beams of $He^+$. The diameter of the ion beam was about 4 cm. The beam current was at a level of 300 μA for the cross-sectional area of the ion beam of about 30 cm$^2$. The beam current density was at a level of about 9 μA/cm$^2$. The working pressure in the vacuum chamber was at a level from 2 to $5 \times 10^{-3}$ Pa. Two sets of the investigated samples were irradiated. One set was irradiated at room temperature, but the ion beam heated the irradiated samples to about 175 °C. The second set was irradiated at a temperature of 400 ± 20 °C. Half of each irradiated sample was shielded from the ion beam.

## 3. Results

### 3.1. DFT calculations

Table 3 shows the properties of both structures with the addition of 12.5 at.% of zirconium in relation to tungsten. However, according to the experimental observations [23,43], in the case of the P6/mmm structure, a defect was introduced in the form of vacancies caused by the loss of boron and tungsten during deposition.

Kelvin moduli $K_i$ analysis shows that they have positive values in both cases, which confirms their mechanical stability. Both structures are also thermally stable, which results from negative values of the enthalpy of formation. Analysed compounds have hardness close to 26 GPa, however, in the case of the ω phase, the addition of zirconium caused a decrease in theoretical hardness from 34.27 GPa. At the same time, in both cases fracture toughness has a relatively high value of ~ 4.6 MPa$\sqrt{m}$. Analysis of the Poisson's ratio $\nu$ and the G/B Pugh's modulus shows an increase of those parameters and according to the criteria presented in [44] both structures possess the transitional brittle-ductile nature. The density ρ = 11.258 g/cm$^3$ for $P6_3$/mmc and ρ = 11.225 g/cm$^3$ for P6/mmm samples is relatively high, which is important for materials used for radiation shielding. In both cases, thermal conductivity λ = 1.912 W/m•K for $P6_3$/mmc and λ = 1.937 W/m•K is also relatively high in comparison with other ceramics, which may be necessary for heat dissipation during operation in the reactor.

### 3.2. Microstructural characterization

SEM images of coatings on LW and LP substrates show no significant differences in the morphology of the layers (Fig. 1). In Figure S1 in the supplementary materials section, pictures of the as-printed Inconel 617 substrates are presented. LP and LW samples represent similar microstructures, with approximately the same grain size and molybdenum and chromium-rich precipitates alongside grain boundaries.

SEM images of top-view and cross-view coatings, paired with the EDS analysis are presented in Fig. 1. The thickness of the layers

**Table 3**
DFT calculations results of W-Zr-B coatings: chemical formula; proportion of Zr dopant: Zr/(W + Zr); volume per atom; density ρ; formation enthalpy $\Delta_f H$; cohesive energy $E_c$; thermal conductivity λ; Lattice parameters and cell angles; Kelvin moduli $K_i$; elastic constants $C_{ij}$; bulk modulus B; shear modulus G; Young's modulus E; Poisson's ratio ν; hardness $H_v$; fracture toughness $K_{IC}$; reduced Young modulus E*; G/B Pugh's modulus ratio; plasticity index $H_v/E^*$, resistance of plastic deformation $Hv^3/E^2$ of W-Zr-$B_2$ phases: hP6-$P6_3$/mmc-space group, no.194 and defected hP3-P6/mmm-space group, no. 191.

| *$P6_3$/mmc – No. 194* | | | | *P6/mmm – No.191 (defected)* | | | |
|---|---|---|---|---|---|---|---|
| $W_{0.875}Zr_{0.125}B_2$ | | | | $W_{0.857}Zr_{0.143}B_2$ | | | |
| ***Source*** | ***Value*** | ***Source*** | ***Value*** | ***Source*** | ***Value*** | ***Source*** | ***Value*** |
| Zr/(Zr+W) | 1/8 | $C_{11}$ (GPa) | 541.560 | Zr/(Zr+W) | 1/7 | $C_{11}$ (GPa) | 638.182 |
| Vol/atom | 9.533 | $C_{22}$ (GPa) | 532.753 | Vol/atom | 9.479 | $C_{22}$ (GPa) | 616.863 |
| $\rho$ (g /cm$^3$) | 11.258 | $C_{33}$ (GPa) | 852.923 | $\rho$ (g /cm$^3$) | 11.225 | $C_{33}$ (GPa) | 505.912 |
| $-\Delta_f H$ (eV/at) | 0.438 | $C_{44}$ (GPa) | 231.813 | $-\Delta_f H$ (eV/at) | 0.425 | $C_{44}$ (GPa) | 236.073 |
| $-E_c$ (eV/at) | 8.583 | $C_{55}$ (GPa) | 229.596 | $-E_c$ (eV/at) | 8.536 | $C_{55}$ (GPa) | 233.391 |
| ***a*** (Å) | 7.760 | $C_{66}$ (GPa) | 166.800 | ***a*** (Å) | 6.036 | $C_{66}$ (GPa) | 241.134 |
| ***b*** (Å) | 5.831 | $C_{12}$ (GPa) | 200.813 | ***b*** (Å) | 6.043 | $C_{12}$ (GPa) | 154.256 |
| ***c*** (Å) | 10.111 | $C_{13}$ (GPa) | 111.130 | ***c*** (Å) | 6.259 | $C_{13}$ (GPa) | 194.818 |
| α (°) | 90.00 | $C_{23}$ (GPa) | 112.813 | α (°) | 89.83 | $C_{23}$ (GPa) | 195.697 |
| β (°) | 90.00 | ***B*** (GPa) | 305.66 | β (°) | 89.56 | ***B*** (GPa) | 315.23 |
| ***ϒ*** (°) | 90.00 | ***G*** (GPa) | 218.50 | ***ϒ*** (°) | 60.69 | ***G*** (GPa) | 220.83 |
| cell volume | 457.574 | ***E*** (GPa) | 529.36 | cell volume | 199.062 | ***E*** (GPa) | 537.23 |
| λ (W/m•K) | 1.912 | ***ν*** | 0.21 | λ (W/m•K) | 1.937 | ***ν*** | 0.22 |
| $K_I$ (GPa) | 963.910 | $H_v$(GPa) | 26.16 | $K_I$ (GPa) | 954.279 | $H_v$ (GPa) | 25.89 |
| $K_{II}$ (GPa) | 627.050 | $K_{IC}$(MPa•m$^{1/2}$) | 4.52 | $K_{II}$ (GPa) | 493.506 | $K_{IC}$ (MPa•m$^{1/2}$) | 4.68 |
| $K_{III}$ (GPa) | 463.626 | $E^*$ (GPa) | 553.78 | $K_{III}$ (GPa) | 485.974 | $E^*$ (GPa) | 564.31 |
| $K_{IV}$ (GPa) | 459.192 | $B/G$ | 1.40 | $K_{IV}$ (GPa) | 465.791 | $B/G$ | 1.43 |
| $K_V$ (GPa) | 336.276 | $H_v/E^*$ | 0.047 | $K_V$ (GPa) | 448.814 | $H_v/E^*$ | 0.046 |
| $K_{VI}$ (GPa) | 333.599 | $H_v^3/E^2$ GPa) | 0.059 | $K_{VI}$ (GPa) | 333.79 | $H_v^3/E^2$ (GPa) | 0.054 |

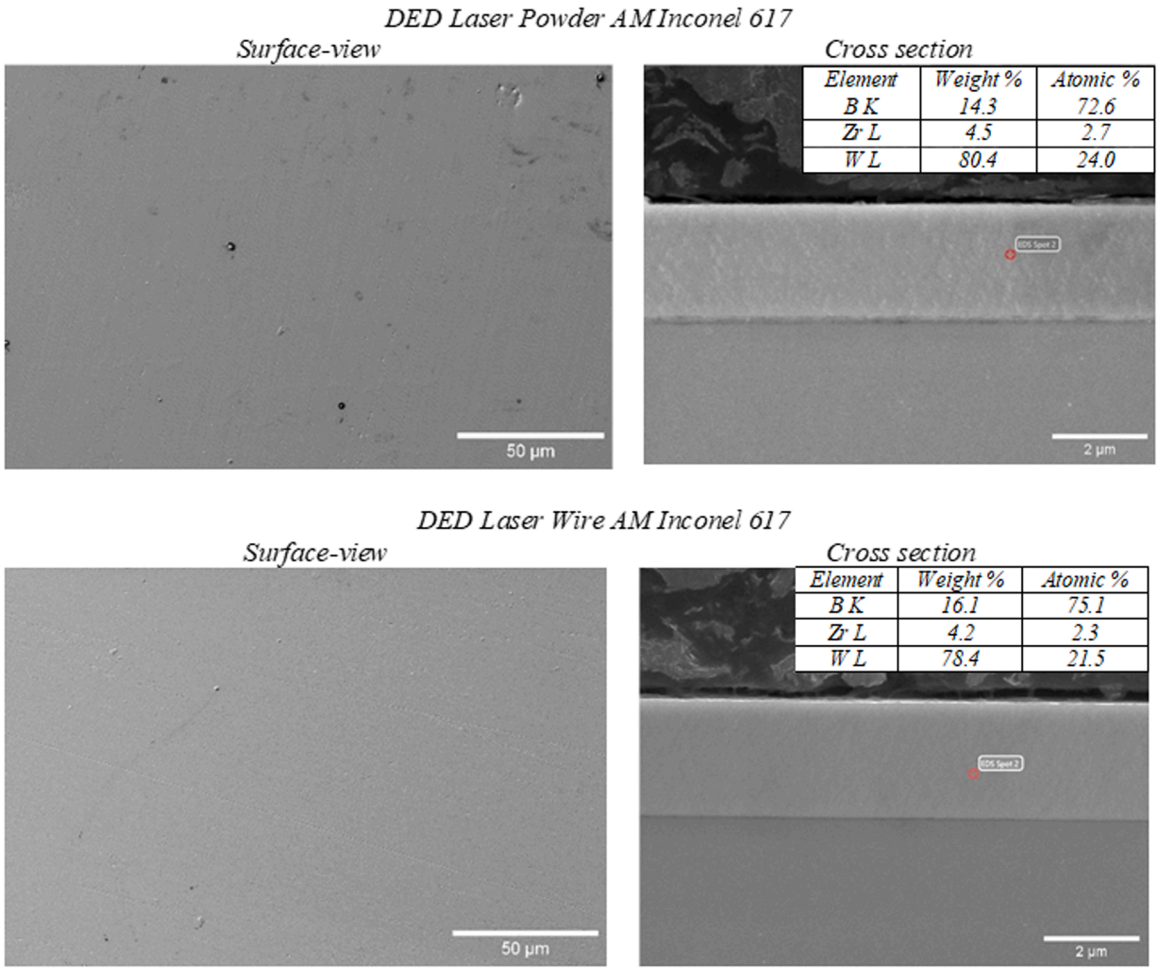


**Fig. 1.** Surface-view and cross-section SEM images and EDS analysis of the W-Zr-B coatings formed at Laser Powder and Laser Wire DED AM Inconel 617 substrates.

deposited at the LP substrate was ca. 2.40 µm, and for the LW substrate was ca. 2.50 µm. Judging from the SEM-EDS chemical composition analysis for compositions acquired for differently manufactured samples, no significant differences can be observed. Atomic concentrations of boron, zirconium, and tungsten are similar, with only slight changes between both samples. For instance, the atomic zirconium concentration for coating deposited on LW AM Inconel 617 is 2.3 at.% and for coating deposited on LP AM Inconel 617 is 2.7 at.%. Results obtained using SEM-EDS, differ from the atomic concentration of the target used to deposit coatings. For instance, the zirconium atomic concentration of the target was approximately 4.5 at.%, while for the synthesized coatings measured value of zirconium concentration was 2.7 at.% and 2.3 at.%. Additionally, higher boron concentrations were observed for both of the samples, compared to theoretical values.

The TEM investigation results are shown in Fig. 2. Fig. 2a and 2b provide a clear comparison of the interface morphology between LP HT and LW HT samples. These Figures reveal good adhesion of the film to the substrate and featureless structure of the coatings, which is typical for amorphous films deposited by magnetron sputtering. The amorphous structure is confirmed by the acquired SEAD pattern in Fig. 2c. Moreover, Fig. 2d shows the layer and interface between the film and substrate (additively manufactured Inconel 617). The adhesion of deposited films seems to be good in both studied samples. The deformed area of the substrate is approximately 700 nm.

TEM microstructural investigations of the coatings after ion implantation at room temperature and 400 °C are presented in Fig. 3. Fig. 3a, b, c, d show general images of the damaged near-surface layers. The thickness of the damaged area in both samples is approximately the same, about 310 nm. Significant swelling is visible near the surface, up to 100 nm depth. High magnification TEM images were taken in the pristine areas (Fig. 3f and h) and in the peak damage area (centre of the images approximately at 150 nm from the surface) after helium implantation (Fig. 3e and g). The images were taken in under-focus conditions to highlight the presence of helium bubbles. The images of irradiated areas clearly show the evolution of the microstructure under helium irradiation. The high magnification TEM images of the pristine areas show a dense and featureless microstructure of deposited thin films. The microstructure observations after helium implantation reveal helium bubbles of slightly less than 1 nm in diameter. The helium bubbles are homogeneously distributed in the peak damage areas. The damage caused by helium is slightly more pronounced after irradiation at room temperature. Following conclusion has been confirmed by the helium bubble size distribution measurements of helium bubbles, which results are presented in Fig. 4 and Table 4 For the coating ion-implanted in room temperature on LP substrate average size of 0.77 nm whereas for the sample on the same substrate implanted in 400 °C average size of helium bubble was 0.54 nm. Moreover, number density of helium bubbles was $1.05 \times 10^{23}$ $m^{-3}$ for the LP RT sample and $1.50 \times 10^{23}$ $m^{-3}$ for the LP HT sample. Similar relationship in helium bubble size was observed in coating deposited on the LW substrate. Bubbles occurring after ion-implantation at room temperature tend to be slightly larger (0.512 nm) compared to those created after ion-implantation at 400 °C (0.467 nm). Helium bubble density was higher in general, in LW samples than LP samples, however higher bubble density was observed in LW RT sample compared to the LW HT sample. Nevertheless, overall these density differences were minor. It should be noted that cracking related

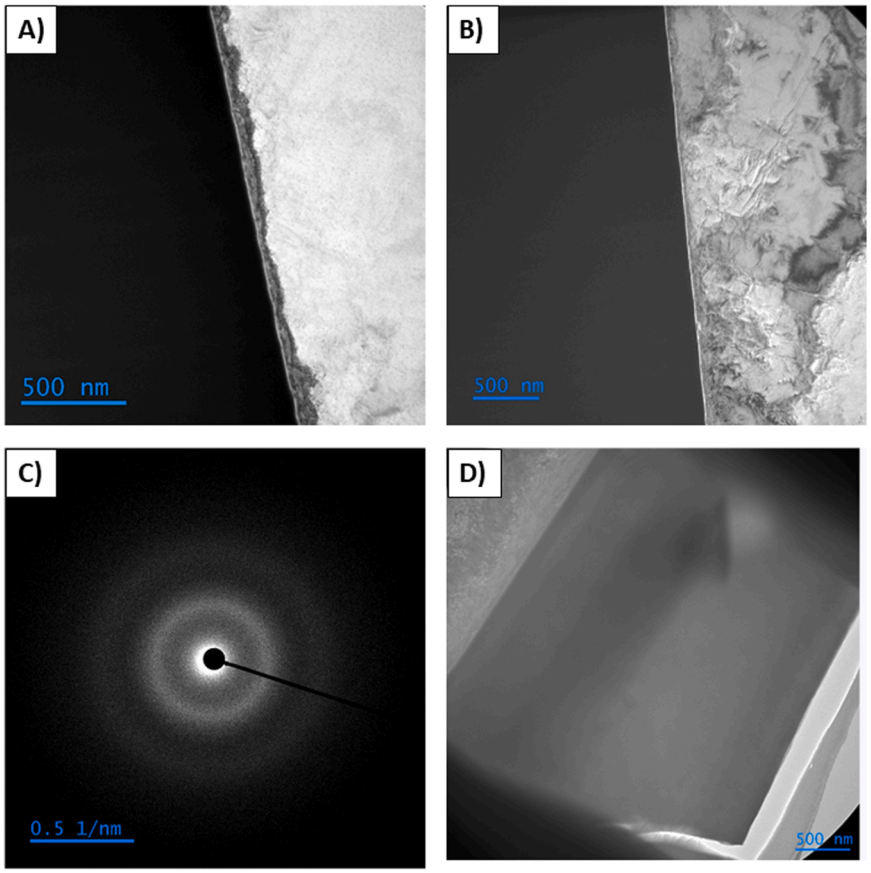


**Fig. 2.** TEM images of the interface layer-substrate: a) LP sample irradiated at HT, b) LW sample irradiated at HT, c) SAED pattern of amorphous thin film, d) TEM bright field image of deposited thin film and substrate-layer interface.

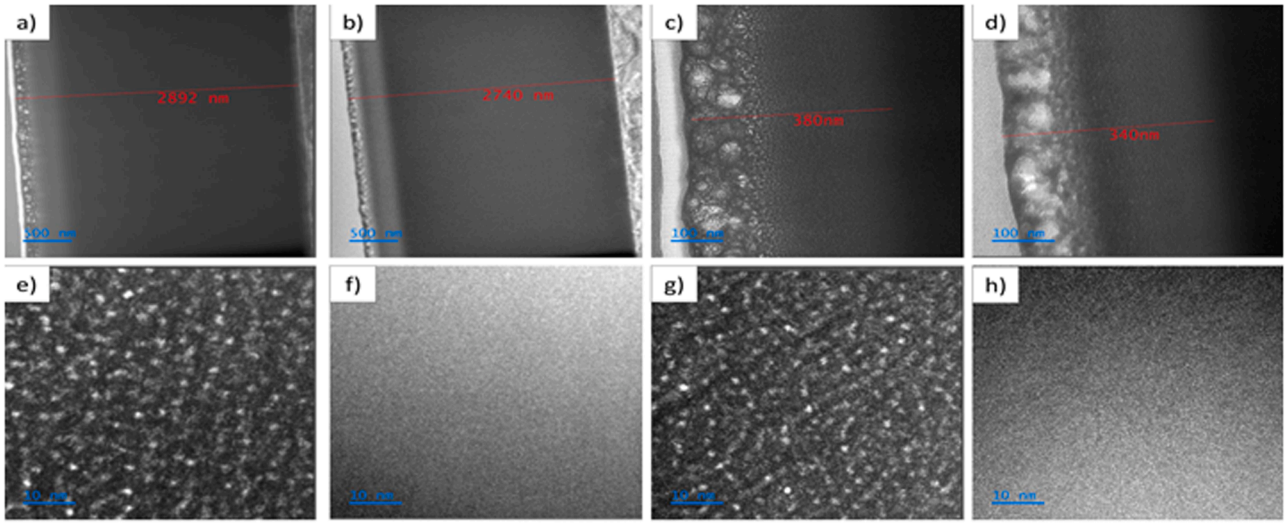


**Fig. 3.** TEM images of radiation damaged W-Zr-B layer deposited on the LW substrate: a) general view of the layer irradiated at RT, b) general view of the layer irradiated at HT, c) higher magnification image of layer irradiated at RT, d) higher magnification image of irradiated layer at HT, e) under focus image of peak damage area (RT), f) under focus image of pristine area (RT), g) under focus image of peak damage area (HT), h) under focus image of pristine area (HT).

to the formation of the bubbles was not observed in the studied layers. It is because thin films fabricated in this paper exhibit an amorphous structure. According to Gutierrez et al [25], amorphous materials have a significantly better resistance to cracking under helium irradiation than crystalline ones. Radiation-induced defects, which are commonly occurring in crystalline materials, such as vacancies, dislocations or interstitial atoms, lead to material hardening and its vulnerability to cracking [45]. Ion irradiation of amorphous layers mostly generates the voids which are created by vacancies and displacement of atoms which undergo short-range ordering [46,47], and in a result swelling and hardness loose are mostly observed effects. In our case, the effect of crystal grains clusters was not observed, which means the W-Zr-B layers are structurally stable during irradiation even at 400 °C, but nevertheless nanohardness tends to drop.

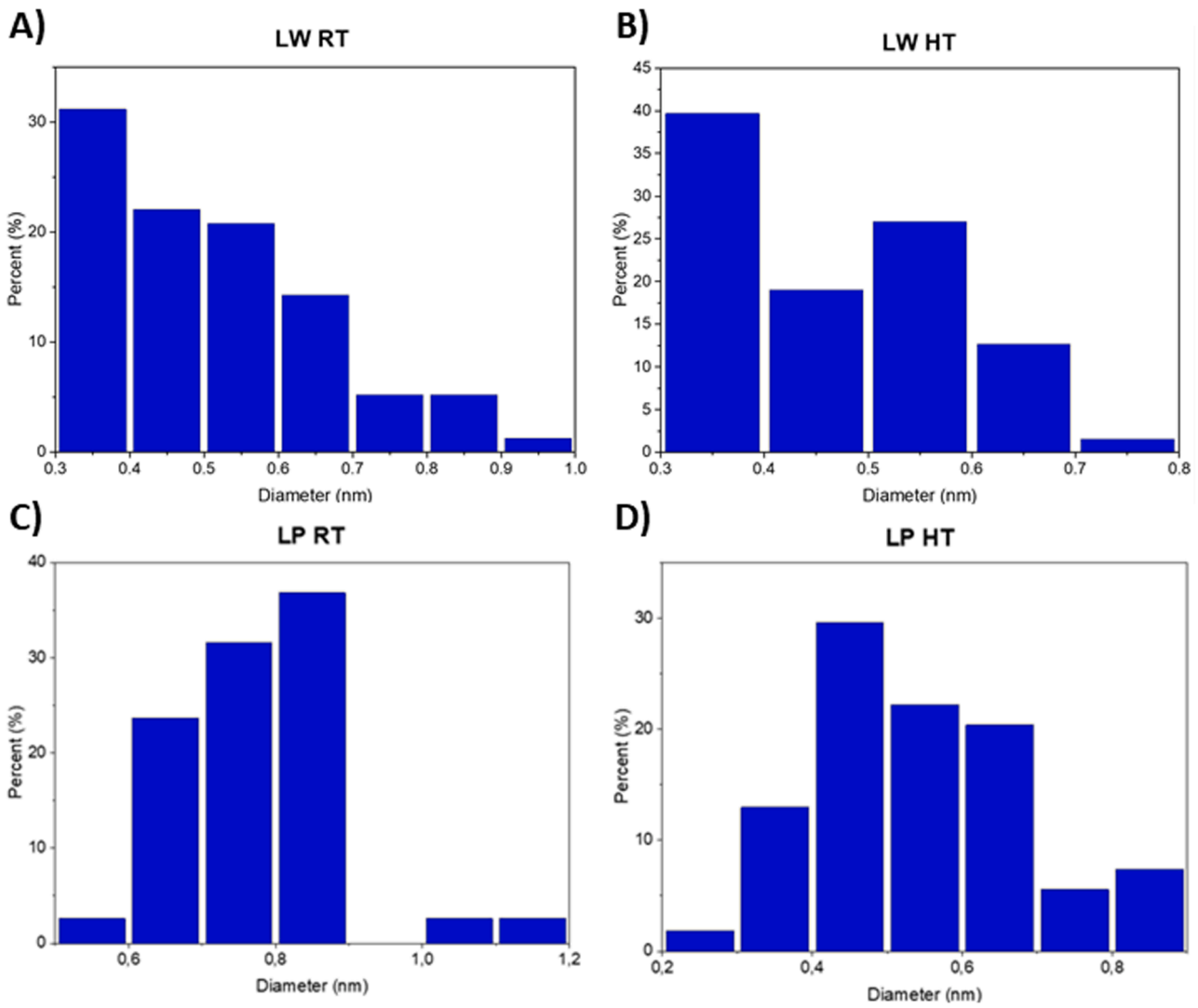


**Fig. 4.** Distribution of helium bubbles size in $W_{0.84}Zr_{0.16}B_{2.5}$ layers deposited on Inconel 617 after different helium-ion implantation conditions: a) LW substrate implanted at RT, b) LW substrate implanted at HT (400 °C), c) LP substrate implanted at RT, d) LP substrate implanted at HT (400 °C).

**Table 4**
Average helium bubbles size and number density for different helium-ion implantation conditions.

| *Implanted substrate* | *Helium bubbles size* | | | |
|---|---|---|---|---|
| | *LW RT* | *LW HT 400 °C* | *LP RT* | *LP HT 400 °C* |
| ***Average [nm]*** | *0.512* | *0.467* | *0.774* | *0.544* |
| ***St. dev. [nm]*** | *0.145* | *0.120* | *0.117* | *0.142* |
| ***Number density [m$^{-3}$]*** | *$2.14 \times 10^{23}$* | *$1.75 \times 10^{23}$* | *$1.05 \times 10^{23}$* | *$1.50 \times 10^{23}$* |

### 3.3. Adhesion of the W-Zr-B layers

Fig. 5 presents values of critical loads measured during the scratch test. $L_{c1}$ and $L_{c2}$ values are similar in both analysed samples, respectively 2.1 N and 3.4 N for the LW sample and 1.9 N and 3.6 N for the LP sample. However, for the $L_{c3}$ value, a slightly higher difference was observed, $L_{c3}$ value for the LW sample was 6.6 N and 5.4 N for the LP sample. Furthermore, in Fig. 6, optical microscope images of the scratch test trails and in Fig. 7, progressive load scratch test data for both samples are presented. Both microscope images and progressive load data show no significant differences between coatings deposited on differently

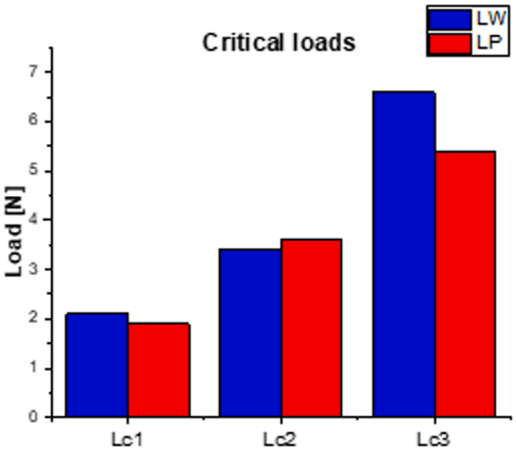


**Fig. 5.** Critical loads values determined during scratch tests of $W_{0.84}Zr_{0.16}B_{2.5}$ layer deposited on LW (blue bars) and LP (red bars) AM Inconel 617, where: $L_{c1}$ – first cracks in coatings, $L_{c2}$ – spallation/chipping at the edge/border of the scratch-track, $L_{c3}$ spallation/chipping through the width of the scratch-track.

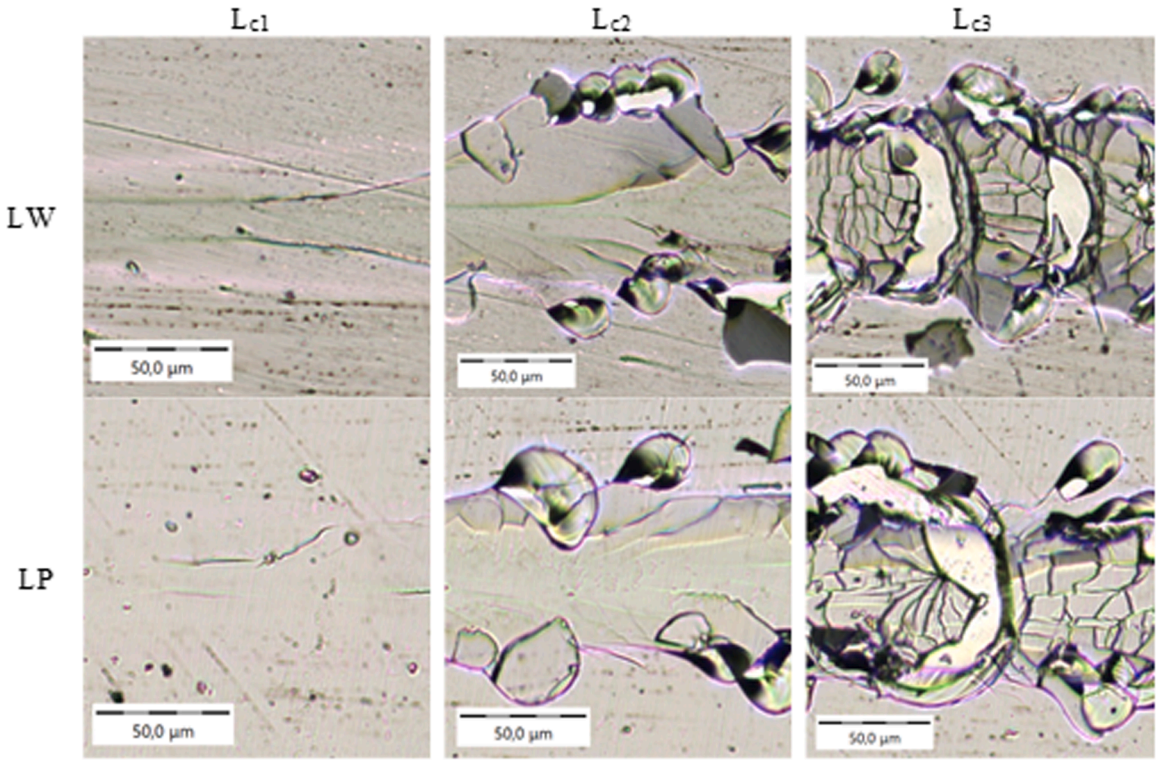


**Fig. 6.** Optical micrographs of the $W_{0.84}Zr_{0.16}B_{2.5}$ layer surface deposited on LW and LP AM Inconel 617, corresponding to the critical load values from Fig. 5.

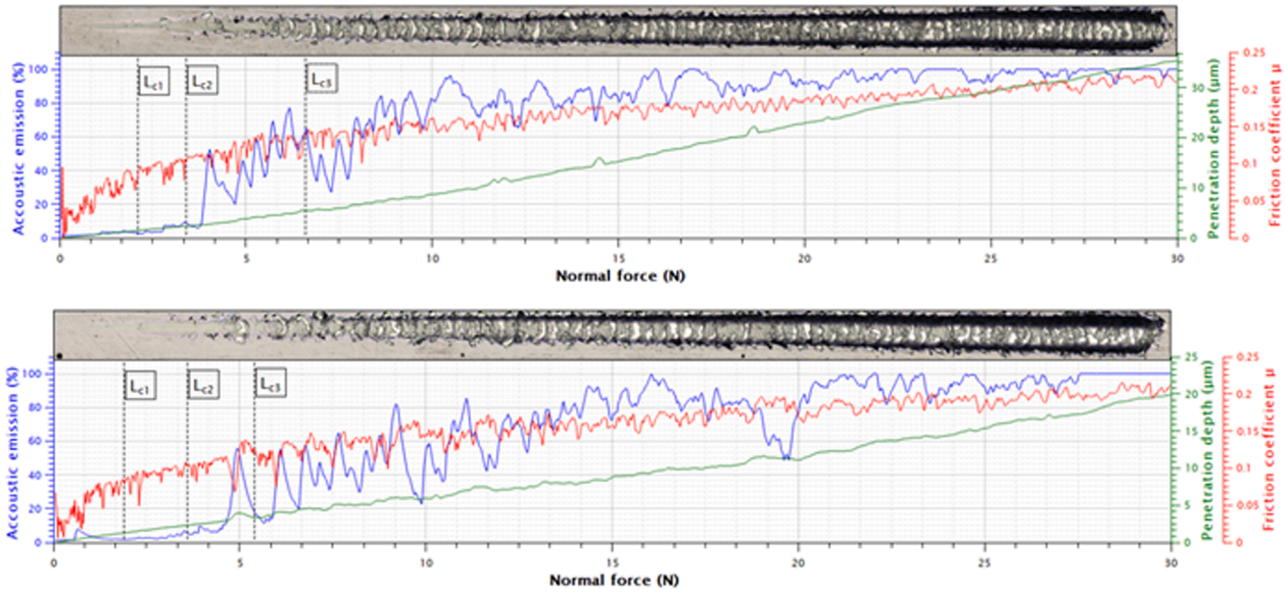


**Fig. 7.** Progressive load scratch test data for a $W_{0.84}Zr_{0.16}B_{2.5}$ films deposited on a LP AM Inconel 617 (top picture) and on a LW AM Inconel 617 (bottom picture) substrate, synchronized to the dataset and critical failure points (panorama magnification 800x).

manufactured substrates.

### 3.4. Simulation of ion irradiation

Fig. 8 presents the modelled depth (red) and damage (black) profile for $He^+$ in W-Zr-B substrate for the fluence of $5 \times 10^{17}$ $cm^{-2}$ and the energy of 60 keV. The peak volume dopant concentration $N_{max}$ for helium ions depth profile is $3.18 \times 10^{22}$ $cm^{-3}$. The projected range $R_p$ and the range straggling $\Delta R_p$ are 167.7 nm and 122.4 nm, respectively. The skewness and the kurtosis are -0.35 and 2.63, respectively, rounded to 2 decimal places. The maximum value of the displacement per atom is 11.3 dpa. This value is located at a depth of 145 nm.

### 3.5. Mechanical properties

To investigate and examine the influence and damage induced by helium bubbles on the behaviour of the thin films, nanoindentation examination . In Fig. 9, graphs demonstrating hardness as a function of depth for the coatings on LW and LP AM Inconel 617 substrates are presented. To obtain the response only from the irradiated zone of the

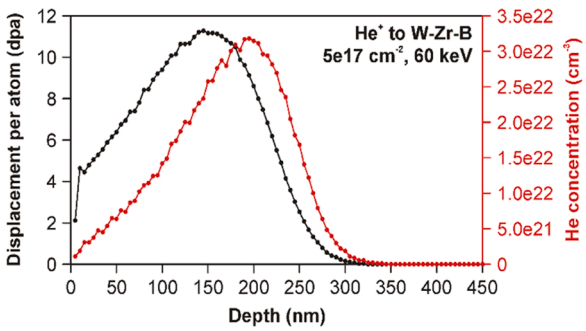


**Fig. 8.** Modelled depth (red) and damage (black) profile for $He^+$ in W-Zr-B substrate for the fluence of $5 \times 10^{17}$ $cm^{-2}$ and the energy of 60 keV.

W-Zr-B film, the smallest possible load of 1 mN was chosen to minimize depth of indentation. Furthermore, in Table 5, measured hardness of the samples is presented. For the virgin samples, measured hardness was 21.12 GPa for LP sample and 19.15 GPa for LW sample. The implantation process lead to a significant decrease in the hardness of both samples. After implantation at room temperature, hardness was 6.51 GPa for the LW sample and 7.83 GPa for the LP. Implantation in 400 °C caused slightly smaller decrease in coatings hardness, 9.40 GPa for the LW sample and 9.71 GPa for the LP sample.

## 4. Discussion

Windsor et al [12] show tungsten boride is a good candidate for shields in a spherical tokamak fusion power plant. Especially, $W_2B_5$ gave the most favourable results with a factor of ~10 or greater reduction in neutron flux and gamma energy deposition as compared to monolithic tungsten. However, this material as a ceramic, is relatively brittle. As ab initio calculation and experimental studies have shown, introducing an alloying element of zirconium can improve this property while maintaining very high hardness [23] and, at the same time, has a positive effect on the thermal stability of this compound [43]. Due to the mechanical properties (the best ratio of hardness to fracture toughness) determined based on experimental studies, the addition is about 12 at.% concerning the amount of tungsten [43]. Tungsten diboride prefers a $W_2B_{5-x}$ based structure (ω, space group 194 - $P6_3/mmc$) due to the highest negative formation enthalpy. Regarding the synthesis via magnetron sputtering, it is a well-known fact that metastable structures (α, space group 191-P6/mmm) can be captured via this synthesis route [48], which is often achieved by implementing point defects such as vacancies. Due to the different arrangement of atoms and consequently a large number of covalent bonds in relation to ionic (metallic) bonds, the undoped $W_2B_{5-x}$ phase has a very high hardness (34.27 GPa) and is brittle [49] at the same time (low Poisson's ratio $\nu = 0.19$ and Pugh's ratio $B/G = 1.3$), while the α phase (space group 191-P6/mmm) is characterized by a much lower hardness of 21.18 GPa but is at the same time more ductile [23].

The thickness values of the films obtained in this paper are comparable to those obtained for similar layers in different papers [23,20]. Furthermore, no delamination of the coating was observed. It is especially important since the films were deposited on AM Inconel 617, which is a relatively low-hardness material. The deformation of the substrate up to the depth of 700 nm is visible on the TEM images (Fig 2). Results obtained using SEM-EDS differ from the atomic concentration of the target used to deposit coatings. For instance, the zirconium atomic concentration of the target was approximately 4.5 at.%, while for the synthesized coatings measured value of zirconium concentration was 2.7 at.% and 2.3 at.%. According to the hypothesis by C. Fuger et. al. in $TiB_{2+x}$ coatings, the Ti/B ratio can be modified by varying the sputtering angle and distance from the substrate, as the sputtered boron flux moves normally to the target surface, while heavier Ti is preferentially sputtered at an angle [50]. A similar effect occurs in the investigated layers, where the zirconium flux can be deposited at different angles and thus achieve a lower concentration in the layer. SEM-EDS results prove that HiPIMS, allows fabrication of repeatable coatings. Furthermore, TEM images exhibit that the structure of the coating is featureless and amorphous. Despite the use of the HiPIMS method, which, thanks to the high energy of ions, allows for lowering the temperature at which crystalline boride layers can be obtained, the additional heating above 400 °C is needed for such kind of films [44]. However, microstructure observations of coatings confirms, that HiPIMS coating method used in this paper allows to manufacture dense and homogeneous amorphous coatings [51–54]. TEM observations reveal that the damage layer by helium ion irradiation is approximately 310 nm (Fig. 3). It is slightly higher than the value of 300 nm predicted using SRIM calculations (Fig. 7). The formation of the helium bubbles, especially near the surface, led to the swelling and therefore a slight increase of thickness of the thin films. Hence, the results of the SRIM calculations were not very precise since they cannot predict changes in the dimensions of the layer due to swelling. It should be noted that according to the literature, amorphous structures have larger capacities accommodating helium

**Table 5**
Nanohardness of the W-Zr-B coatings deposited on the Inconel 617 LW and LP virgin samples and irradiated at room temperature (RT) and 400 C°.

| *AM Inconel 617 substrate* | *W-Zr-B coatings hardness [GPa]* | | |
|---|---|---|---|
| | *Virgin* | *Irradiated at RT* | *Irradiated at 400 °C* |
| ***LW*** | 19.15 ± 0.63 | 6.51 ± 0.29 | 9.40 ± 0.63 |
| ***LP*** | 21.12 ± 1.29 | 7.83 ± 0.79 | 9.71 ± 0.74 |

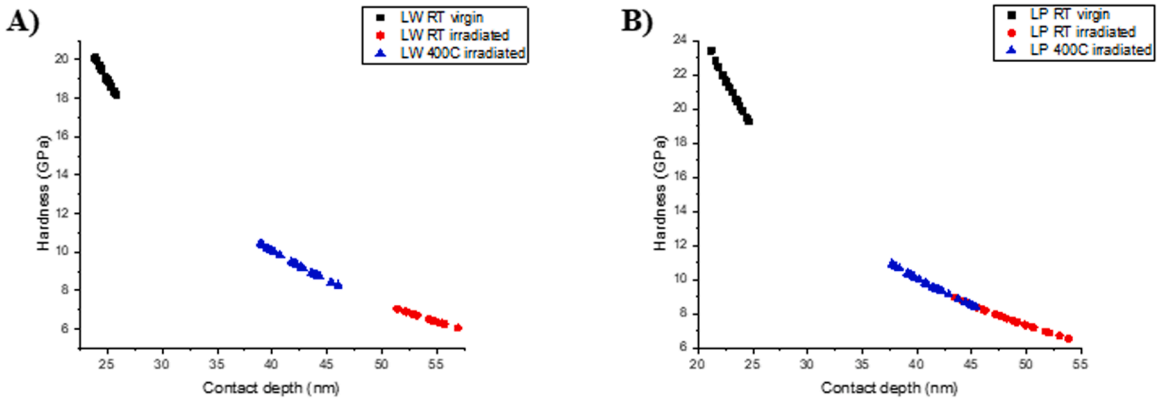


**Fig. 9.** Hardness as a function of depth of the W-Zr-B coating deposited on the: A) LW AM Inconel 617, B) LP AM Inconel 617. Samples before (virgin) and after ion implantation (irradiated) measured at 1mN load. Samples were implanted at room temperature (RT irradiated) and 400 °C (400 C irradiated).

atoms than crystalline structures [25]. There is no noticeable difference between the thickness of the irradiated layer at RT and 400 °C. It seems that 400 °C is too low to significantly enhance the mobility of helium atoms and to increase the irradiated area. However, according to the study by Zdorovets et al [54], who irradiated ceramic thin film at RT and 727 °C, found that the layer formed during irradiation at HT is slightly wider. Nevertheless, it has been proven that helium bubbles in samples irradiated at room temperature tend to be larger, but they occur in lower quantities, than in samples irradiated at 400 °C. Our findings are not fully consistent with those of Shen et al [55]. They have implanted High Entropy Alloys at different temperatures, and results showed that an increase in temperature led to increased in the size of helium bubbles. They have supposed that increase in irradiation temperature caused increase in He atoms diffusion energy, which induced formation of bigger helium bubbles. Nevertheless, the results obtained in this paper exhibit a high degree of similarity to those reported by others [56–58]. Tynyshbayeva et al. examined the helium swelling phenomenon in SiC ceramics and determined that in SiC ceramics helium implantation-induced damage consists of two stages, the first one is related to the local crystallization that leads to generation of dislocations, causing brittleness of the material [59]. The second stage involves swelling formation of bubbles near the surface and hardness drop, which was observed in W-Zr-B coatings analysed in this paper. However, most of the attention is drawn to crystalline ceramics, regarding the irradiation resistance, therefore mechanisms underlying helium bubbles growth and formation in W-Zr-B ceramics are still not fully understood and should be further investigated.

Coatings deposited on differently manufactured substrates behave similarly during scratch-test. We can observe the combination of tensile, Hertzian circular and conformal cracks in both cases. Spallation at the borders of the scratch tracks seems to be mainly cohesive. Despite low critical loads, presented in Fig. 5, in comparison with Mościcki et al [60] we do not observe gross spallation. In general adhesive type of failure seems to be relatively minor, additionally all types of damage are only occurring in close proximity of the track borders. In both cases penetration depth exceeded the thickness of the coatings, see Figs. 6,7 without complete delamination of the coatings. Low fracture toughness of the coatings and high adhesion to substrates may be the main reason for the mostly cohesive type of failure during scratch-test. In Fig. 6 we present the close-ups of the areas where critical loads ($L_{cx}$) occurred.

Zirconium-doped tungsten boride coatings synthesized using HiPIMS in this paper exhibit a substantial hardness of 21 GPa. Results obtained here are comparable to those obtained by others. For instance, Garbiec et al. achieved 18.1 GPa HV hardness for $W_{0.84}Zr_{0.16}B_{2.5}$ fabricated using SPS method [21]. Moreover, Maździarz et al. also fabricated zirconium-doped tungsten boride coatings using magnetron sputtering at different zirconium concentrations [23]. For the concentration similar to the one fabricated in this paper, they have achieved layer hardness of about 33 GPa HV. Furthermore, Psiuk et al. and Mościcki et al. manufactured W-Zr-B coatings and have reached hardness varying from 20 to 40 GPa [20,24]. In all mentioned cases, the higher hardness was a result of crystalline microstructure obtained due to higher deposition temperature (540 °C). Based on the mentioned results obtained by others, it can be stated that the HiPIMS method used in this paper is a reliable technique for fabricating zirconium-doped tungsten boride coatings, with extraordinary properties. The helium ion implantation in metallic crystalline thin films [61] and metallic bulk materials [8] causes a hardness increase. This is related to the fact that the created helium bubbles act as obstacles to dislocation movements, increasing hardness. However, for ceramic amorphous or crystalline thin films, the helium ion irradiation causes instead a decrease of hardness due to minimal strain hardening capacity, which does not counteract the influence of voids and bubbles on the hardness. The softening of ceramic materials after helium irradiation was observed in the literature [6,54,62,63]. Therefore, judging from the conducted TEM observations of the irradiated coatings, helium swelling and bubbles might be the leading cause of the significant hardness decrease after ion implantation. A slightly higher degree of damage was observed in the damaged zone in the samples irradiated in RT, which led to a higher decrease in hardness than in the samples irradiated at 400 °C. Zdorovets et al. studied a degradation process of helium ions implanted crystalline aluminium-based nitride ceramics [54]. They, similarly to our research, observed a decrease in coatings hardness after the irradiation process. Furthermore, the decrease in hardness was higher for the samples irradiated at RT, which fully corresponds with the results obtained in this paper.

## 5. Conclusions

Zirconium – doped tungsten boride coatings ($W_{0.84}Zr_{0.16}B_{2.5}$) were successfully synthesized on additively manufactured Inconel 617 substrate using High Power Impulse Magnetron Sputtering (HiPIMS) method, and their microstructure, chemical composition, adhesion to the surface and irradiation resistance was evaluated. DFT calculations were performed to determine theoretical thermal and mechanical properties and density. Coatings manufactured using HiPIMS are amorphous, approximately 2.5 μm thick, with good adherence to the surface. Furthermore it has been proven that different feedstock, laser or powder of AM Inconel 617, does not influence properties of fabricated $W_{1-x}Zr_xB_{2.5}$ coatings. SEM and TEM images showed that the coatings are uniform and featureless. Microscopic analyses of the peak damage area of the implanted coatings revealed helium bubbles not exceeding 1 nm in diameter (0.54–0.77 nm range), which is comparable to results obtained by others. The chemical composition of the films was similar between coatings manufactured on the different substrates, however some more precise method than SEM-EDS to demonstrate their accurate composition is need to be implemented in future works. Scratch-test results indicate that despite low critical loads, the coatings exhibit good adhesion to the substrate, regardless of the substrate additive manufacturing parameters. The hardness of the pristine coatings does not differ on the different substrates, and the hardness of similar composition coatings obtained in other research. After ion implantation hardness of the coatings decreased from 21.12 GPa (LP) and 19.15 GPa (LW) to 6.51 GPa (LW) and 7.83 GPa (LP) for coatings irradiated at room temperature. After irradiation at 400 °C, the hardness of the obtained coatings was 9.40 GPa (LW) and 9.71 GPa (LP). Nanoindentation results, combined with TEM observations and helium bubble size measurements, confirmed that the presence of helium bubbles results in softening of the W-Zr-B coatings deposited on additively printed Inconel 617 substrate. Furthermore, it proved that an increase in the dimensions of helium bubbles led to a further decrease in W-Zr-B coating hardness. Most probable cause of such behaviour is voids, which trigger the swelling phenomenon. Based on the results obtained, we confirmed that the HiPIMS method makes it possible to produce hard coatings of zirconium-doped tungsten boride with similar chemical composition and properties. However, based on the irradiation effects results, studies on their beneficial application as shielding materials and irradiation resistant systems should still be continued and are planned by the authors.

## CRediT authorship contribution statement

**Józef Rzempołuch:** Writing – original draft, Visualization, Investigation, Formal analysis. **Tomasz Stasiak:** Writing – review & editing, Writing – original draft, Investigation, Formal analysis. **Marcin Maździarz:** Visualization, Investigation, Formal analysis. **Jarosław Jasiński:** Writing – review & editing, Writing – original draft, Methodology, Formal analysis, Conceptualization. **Udisien Woy:** Investigation. **Rafał Psiuk:** Visualization, Investigation, Formal analysis. **Marcin Kowal:** Investigation. **Anna Kosińska:** Investigation. **Magdalena Wilczopolska:** Investigation. **Katarzyna Mulewska:** Investigation, Formal analysis. **Marek Barlak:** Investigation, Formal analysis. **Katarzyna**

**Ciporska:** Investigation. **Łukasz Kurpaska:** Supervision, Funding acquisition. **Jacek Jagielski:** Supervision, Funding acquisition. **Tomasz Mościcki:** Writing – review & editing, Writing – original draft, Supervision, Methodology, Investigation, Funding acquisition, Formal analysis, Conceptualization.

## Declaration of competing interest

The authors declare that they have no known competing financial interests or personal relationships that could have appeared to influence the work reported in this paper.

## Acknowledgements

The Authors are thankful to Mr. Jerzy Zagórski for technical assistance with ion implantation processing.

This work was supported by the National Science Centre (NCN, Poland) 2022/47/B/ST8/01296 in the case of DFT calculations. Also scratch tests was made on apparatus funded by this project.

Activities financed within the framework of the undertaking of the Ministry of Education and Science entitled “Technical Description of the Research High-Temperature Gas Cooled Reactor (HTGR)” in the years 2021-2024

SafeG project - Safety of GFR through innovative materials, technologies and processes / Ensuring safe operation of a GFR reactor through the use of advanced materials, technologies and processes. Project implemented under Horizon 2020 Euratom (H2020-Euratom) No. 945041 (project budget - EUR 249,469.00) and supported by the Ministry of Science and Higher Education with the amount of PLN 377,403.00 - contract No. 5168/H2020-Euratom/2021/2 dated 01.03.2022.

The co-authors J. Jasiński, M. Wilczopolska, A. Kosińska, K. Mulewska, Ł. Kurpaska and J. Jagielski, acknowledge the support from the European Union Horizon 2020 research and innovation program under NOMATEN Teaming grant agreement no. 857470 and from the European Regional Development Fund via the Foundation for Polish Science International Research Agenda Plus program grant no. MAB PLUS/2018/8 which partially covered salary during the preparation of this article

The publication was created within the framework of the project of the Minister of Science and Higher Education "Support for the activities of Centres of Excellence established in Poland under Horizon 2020" under contract no. MEiN/2023/DIR/3795

## Supplementary materials

Supplementary material associated with this article can be found, in the online version, at doi:10.1016/j.jnucmat.2025.156091.

## Data availability

Data will be made available on request.

## References

[1] H.Shah Hosseini, M. Shamanian, A. Kermanpur, Characterization of microstructures and mechanical properties of Inconel 617/310 stainless steel dissimilar welds, Mater. Charact. 62 (2011) 425–431, https://doi.org/10.1016/J.MATCHAR.2011.02.003.

[2] W. Ren, R. Swimdeman, A review paper on aging effects in alloy 617 for GEN IV nuclear reactor applications, J. Press. Vessel Technol. Trans. ASME 131 (2009) 024002, https://doi.org/10.1115/1.2967885.

[3] S. Salari, M.S. Rahman, A.A. Polycarpou, A. Beheshti, Elevated temperature mechanical properties of Inconel 617 surface oxide using nanoindentation, Mater. Sci. Eng. A 788 (2020) 139539, https://doi.org/10.1016/j.msea.2020.139539.

[4] X. Zhang, G. Zhai, C. Jiang, L. Wang, Y. Chu, R. Sun, Effect of pre-strain on high-temperature oxidation behavior of inconel 617 superalloy fabricated by wire arc additive manufacturing at 900 °C, J. Mater. Eng. Perform. (2024) 1–10, https://doi.org/10.1007/s11665-024-10405-w.

[5] T. Hassel, T. Carstensen, Properties and anisotropy behaviour of a nickel base alloy material produced by robot-based wire and arc additive manufacturing, Weld. World 64 (2020) 1921–1931, https://doi.org/10.1007/s40194-020-00971-7.

[6] C. Wang, H. Tu, R. Su, J. Gao, B.V. King, D.J. O'Connor, L. Shi, Annealing effects on the structure and hardness of helium-irradiated Cr2AlC thin films, J. Am. Ceram. Soc. 104 (2021) 593–603, https://doi.org/10.1111/JACE.17469.

[7] S.H. Li, J.T. Li, W.Z. Han, Radiation-induced helium bubbles in metals, Material 12 (2019) 1036, https://doi.org/10.3390/ma12071036.

[8] Z. Zhu, H. Huang, J. Liu, Z. Zhu, Helium-induced damage behavior in high temperature nickel-based alloys with different chemical composition, J. Nucl. Mater. 541 (2020) 152419, https://doi.org/10.1016/j.jnucmat.2020.152419.

[9] Z. Zhu, H. Huang, J. Liu, J. Gao, Z. Zhu, Xenon ion irradiation induced hardening in inconel 617 containing experiment and numerical calculation, J. Nucl. Mater. 525 (2019) 32–39, https://doi.org/10.1016/j.jnucmat.2019.07.032.

[10] M.J. Baldwin, R.P. Doerner, Helium induced nanoscopic morphology on tungsten under fusion relevant plasma conditions, Nucl. Fusion. 48 (2008) 035001, https://doi.org/10.1088/0029-5515/48/3/035001.

[11] N. Jamal AbuAlRoos, M.N. Azman, N.A. Baharul Amin, R. Zainon, Tungsten-based material as promising new lead-free gamma radiation shielding material in nuclear medicine, Phys. Med. 78 (2020) 48–57, https://doi.org/10.1016/j.ejmp.2020.08.017.

[12] C.G. Windsor, J.O. Astbury, J.J. Davidson, C.J.R. McFadzean, J.G. Morgan, C. L. Wilson, S.A. Humphry-Baker, Tungsten boride shields in a spherical tokamak fusion power plant, Nucl. Fusion 61 (2021) 086018, https://doi.org/10.1088/1741-4326/ac09ce.

[13] Y. Liu, X. Liu, C. Lai, J. Ma, X. Meng, L. Zhang, G. Xu, Y. Lu, H. Li, J. Wang, S. Chen, Boriding of tungsten by the powder-pack process: phase formation, growth kinetics and enhanced neutron shielding, Int. J. Refract. Met. Hard Mater. 110 (2023) 106049, https://doi.org/10.1016/j.ijrmhm.2022.106049.

[14] D. McAlister, Neutron shielding materials, PG Res. Found. (2016).

[15] C.G. Windsor, J.O. Astbury, J.G. Morgan, C.L. Wilson, S.A. Humphry-Baker, Activation and transmutation of tungsten boride shields in a spherical tokamak, Nucl. Fusion 62 (2022) 36009, https://doi.org/10.1088/1741-4326/ac4866.

[16] Y. Lin, C. Mcfadzean, S.A. Humphry-baker, Oxidation resistance of WB and W 2 B-W neutron shields, J. Nucl. Mater. 565 (2022) 153762, https://doi.org/10.1016/j.jnucmat.2022.153762.

[17] L.E. Pangilinan, C.L. Turner, G. Akopov, M. Anderson, R. Mohammadi, R.B. Kaner, Superhard tungsten diboride-based solid solutions, Inorg. Chem. 57 (2018) 15305–15313, https://doi.org/10.1021/acs.inorgchem.8b02620.

[18] G. Akopov, I. Roh, Z.C. Sobell, M.T. Yeung, L. Pangilinan, C.L. Turner, R.B. Kaner, Effects of variable boron concentration on the properties of Superhard Tungsten Tetraboride, J. Am. Chem. Soc. 139 (2017) 17120–17127, https://doi.org/10.1021/jacs.7b08706.

[19] G. Akopov, M.T. Yeung, C.L. Turner, R. Mohammadi, R.B. Kaner, Extrinsic hardening of superhard tungsten tetraboride alloys with group 4 transition metals, J. Am. Chem. Soc. 138 (2016) 5714–5721, https://doi.org/10.1021/jacs.6b02676.

[20] T. Mościcki, R. Psiuk, J. Radziejewska, M. Wiśniewska, D. Garbiec, Properties of spark plasma sintered compacts and magnetron sputtered coatings made from Cr, Mo, Re and Zr alloyed tungsten diboride, Coatings 11 (2021) 111378, https://doi.org/10.3390/coatings11111378.

[21] D. Garbiec, M. Wiśniewska, R. Psiuk, P. Denis, N. Levintant-Zayonts, V. Leshchynsky, R. Rubach, T. Mościcki, Zirconium alloyed tungsten borides synthesized by spark plasma sintering, Arch. Civ. Mech. Eng. 21 (2021) 1–15, https://doi.org/10.1007/s43452-021-00188-5.

[22] K. Khor, L. Yu, G. Sundararajan, Formation of hard tungsten boride layer by spark plasma sintering boriding, Thin. Solid. Films. 478 (2005) 232–237, https://doi.org/10.1016/j.tsf.2004.07.004.

[23] M. Maździarz, R. Psiuk, A. Krawczyńska, M. Lewandowska, T. Mościcki, Effect of zirconium doping on the mechanical properties of W1-xZrxB2 on the basis of first-principles calculations and magnetron sputtered films, Arch. Civ. Mech. Eng. 22 (2022) 193, https://doi.org/10.1007/s43452-022-00513-6.

[24] R. Psiuk, M. Milczarek, P. Jenczyk, P. Denis, D.M. Jarząbek, P. Bazarnik, M. Pisarek, T. Mościcki, Improved mechanical properties of W-Zr-B coatings deposited by hybrid RF magnetron – PLD method, Appl. Surf. Sci. 570 (2021) 151239, https://doi.org/10.1016/J.APSUSC.2021.151239.

[25] G. Gutierrez, S. Peuget, J.A. Hinks, G. Greaves, S.E. Donnelly, E. Oliviero, C. Jégou, Helium bubble formation in nuclear glass by in-situ TEM ion implantation, J. Nucl. Mater. 452 (2014) 565–568, https://doi.org/10.1016/J.JNUCMAT.2014.06.010.

[26] Y. Xie, X. Huang, A. Raj, X. Li, R. Dhall, M. Balooch, A. Minor, J. Schroers, P. Hosemann, Strengthening of Zr-based metallic glass at low dose helium ion irradiation, J. Nucl. Mater. 592 (2024) 154943, https://doi.org/10.1016/j.jnucmat.2024.154943.

[27] M. Jiang, A. Haq Mir, M. Bahri, Y. Zhang, N. Browning, K. Whittle, M. Patel, Helium bubbles in Gd2Ti2O7 borosilicate glass-ceramic composites, J. Nucl. Mater. 581 (2023) 154424, https://doi.org/10.1016/j.jnucmat.2023.154424.

[28] Q. Su, S. Inoue, M. Ishimaru, J. Gigax, T. Wang, H. Ding, M.J. Demkowicz, L. Shao, M. Nastasi, Helium irradiation and implantation effects on the structure of amorphous silicon oxycarbide, Sci. Rep. 7 (2017) 1–8, https://doi.org/10.1038/s41598-017-04247-x.

[29] Q. Su, H. Ding, L. Price, L. Shao, J.A. Hinks, G. Greaves, S.E. Donnelly, M. J. Demkowicz, M. Nastasi, Rapid and damage-free outgassing of implanted helium from amorphous silicon oxycarbide, Sci. Rep. 8 (2018) 1–9, https://doi.org/10.1038/s41598-018-23426-y.

[30] A. Martin, M. Torrent, R. Caracas, Projector augmented-wave formulation of response to strain and electric-field perturbation within density functional

perturbation theory, Phys. Rev. B 99 (2019) 094112, https://doi.org/10.1103/PhysRevB.99.094112.
[31] E. Zhao, J. Meng, Y. Ma, Z. Wu, Phase stability and mechanical properties of tungsten borides from first principles calculations, Phys. Chem. Chem. Phys. 12 (2010) 13158–13165, https://doi.org/10.1039/c004122j.
[32] F. Jollet, M. Torrent, N. Holzwarth, Generation of projector augmented-wave atomic data: A 71 element validated table in the XML format, Comput. Phys. Commun. 185 (2014) 1246–1254, https://doi.org/10.1016/j.cpc.2013.12.023.
[33] M. Maździarz, T. Moscicki, New zirconium diboride polymorphs-first-principles calculations, Material 13 (2020) 133022, https://doi.org/10.3390/ma13133022.
[34] D.R. Hamann, X. Wu, K.M. Rabe, D. Vanderbilt, Metric tensor formulation of strain in density-functional perturbation theory, Phys. Rev. B - Condens. Matter Mater. Phys. 71 (2005) 1–26, https://doi.org/10.1103/PhysRevB.71.035117.
[35] R. Hill, The elastic behaviour of a crystalline aggregate, Proc. Phys. Soc. A 65 (1952) 349–354, https://doi.org/10.1088/0370-1298/65/5/307.
[36] M. Maździarz, Comment on, The Computational 2D Materials Database: high-throughput modeling and discovery of atomically thin crystals, 2d. Mater. 6 (2019) 2–5, https://doi.org/10.1088/2053-1583/ab2ef3.
[37] E. Mazhnik, A.R. Oganov, Application of machine learning methods for predicting new superhard materials, J. Appl. Phys. 128 (2020) 075102, https://doi.org/10.1063/5.0012055.
[38] A.C. Fischer-Cripps, Critical review of analysis and interpretation of nanoindentation test data, Surf. Coat. Technol. 200 (2006) 4153–4165, https://doi.org/10.1016/j.surfcoat.2005.03.018.
[39] W.C. Oliver, G.M. Pharr, An improved technique for determining hardness and elastic modulus using load and displacement sensing indentation experiments, J. Mater. Res. 7 (1992) 1564–1583, https://doi.org/10.1557/jmr.1992.1564.
[40] James Ziegler - SRIM & TRIM (n.d.), http://www.srim.org/(accessed, 2025. February 3.
[41] E. Wyszkowska, C. Mieszczynski, A.Azarov Kurpaska, W. Chromiński, I. Jóźwik, A. Esfandiarpour, A. Kosińska, D. Kalita, R. Diduszko, J. Jagielski, S.T. Nori, M. Alava, The Fe addition as an effective treatment for improving the radiation resistance of fcc NixFe1-x single-crystal alloys, J. Nucl. Mater. 584 (2023) 154565, https://doi.org/10.1016/j.jnucmat.2023.154565.
[42] I. Betlej, M. Barlak, K. Lipska, P. Borysiuk, P. Boruszewski, Argon ion implantation as a method of modifying the surface properties of wood–Plastic composites, Material 17 (2024) 5347, https://doi.org/10.3390/ma17215347.
[43] T. Mościcki, J. Chrzanowska-Giżyńska, R. Psiuk, P. Denis, K. Mulewska, Ł. Kurpaska, M. Chmielewski, M. Wiśniewska, D. Garbiec, Thermal and mechanical properties of (W,Zr)B2-z coatings deposited by RF magnetron sputtering method, Int. J. Refract. Met. Hard Mater. 105 (2022) 105811, https://doi.org/10.1016/J.IJRMHM.2022.105811.
[44] X. Gu, C. Liu, H. Guo, K. Zhang, C. Chen, Sorting transition-metal diborides: new descriptor for mechanical properties, Acta Mater. 207 (2021) 116685, https://doi.org/10.1016/j.actamat.2021.116685.
[45] K. Ming, C. Gu, Q. Su, D. Xie, Y. Wu, Y. Wang, L. Shao, M. Nastasi, J. Wang, Strength and plasticity of amorphous ceramics with self-patterned nano-heterogeneities, Int. J. Plast. 134 (2020) 102837, https://doi.org/10.1016/J.IJPLAS.2020.102837.
[46] W. Huang, W. Yang, Y. Zhang, L. Zhang, J. Yang, C. Zhan, Layered defects effect of Au-ion irradiation in amorphous Al2O3 coating prepared by pulsed magnetron sputtering, Mater. Today Commun. 46 (2025) 112711, https://doi.org/10.1016/J.MTCOMM.2025.112711.
[47] C. Koroni, T. Olsen, J.P. Wharry, H. Xiong, Irradiation-induced amorphous-to-crystalline phase transformations in ceramic materials, Mater 15 (2022) 5924, https://doi.org/10.3390/MA15175924, 2022Page 5924 15.
[48] V. Moraes, H. Riedl, C. Fuger, P. Polcik, H. Bolvardi, D. Holec, P.H. Mayrhofer, Ab initio inspired design of ternary boride thin films, Sci. Rep. 8 (2018) 1–9, https://doi.org/10.1038/s41598-018-27426-w.
[49] S.F. Pugh, XCII. Relations between the elastic moduli and the plastic properties of polycrystalline pure metals, London, Edinburgh, Dublin Philos. Mag. J. Sci. 45 (1954) 823–843, https://doi.org/10.1080/14786440808520496.
[50] C. Fuger, R. Hahn, A. Hirle, P. Kutrowatz, M. Weiss, A. Limbeck, O. Hunold, P. Polcik, H. Riedl, Revisiting the origins of super-hardness in TiB2+z thin films – Impact of growth conditions and anisotropy, Surf. Coat. Technol. 446 (2022) 128806, https://doi.org/10.1016/j.surfcoat.2022.128806.
[51] R. Ganesan, B.J. Murdoch, J.G. Partridge, S. Bathgate, B. Treverrow, X. Dong, A. E. Ross, D.G. McCulloch, D.R. McKenzie, M.M.M. Bilek, Optimizing HiPIMS pressure for deposition of high-k (k = 18.3) amorphous HfO 2, Appl. Surf. Sci. 365 (2016) 336–341, https://doi.org/10.1016/j.apsusc.2016.01.017.
[52] R. Ganesan, I. Fernandez-Martinez, B. Akhavan, D.T.A. Matthews, D. Sergachev, M. Stueber, D.R. McKenzie, M.M.M. Bilek, Pulse length selection in bipolar HiPIMS for high deposition rate of smooth, hard amorphous carbon films, Surf. Coat. Technol. 454 (2023) 129199, https://doi.org/10.1016/j.surfcoat.2022.129199.
[53] H. Fager, G. Greczynski, J. Jensen, J. Lu, L. Hultman, Growth and properties of amorphous Ti-B-Si-N thin films deposited by hybrid HIPIMS/DC-magnetron co-sputtering from TiB2 and Si targets, Surf. Coat. Technol. 259 (2014) 442–447, https://doi.org/10.1016/j.surfcoat.2014.10.053.
[54] M.V Zdorovets, K. Dukenbayev, Study of helium swelling in nitride ceramics at different irradiation temperatures, Material (2019) 12.
[55] H.H. Shen, S.M. Peng, B. Chen, F.N. Naab, G.A. Sun, W. Zhou, X. Xiang, K. Sun, X. T. Zu, Helium bubble evolution in a Zr–Sn–Nb–Fe–Cr alloy during post-annealing: an in-situ investigation, Mater. Charact. 107 (2015) 309–316, https://doi.org/10.1016/J.MATCHAR.2015.07.025.
[56] Y. Zhu, J. Chai, T. Shen, L. Niu, Y. Liu, P. Jin, M. Cui, Y. Feng, L. Sun, Z. Wang, Helium irradiation induced microstructural damages and mechanical response of Al2O3-ZrO2-SiC composites, J. Eur. Ceram. Soc. 43 (2023) 3475–3485, https://doi.org/10.1016/J.JEURCERAMSOC.2023.01.052.
[57] G. Pu, J. Zou, L. Lin, K. Zhang, B. Liu, F. Ma, Q. Wang, Q. Li, Effects of He ion irradiation on the microstructures and mechanical properties of t' phase yttria-stabilized zirconia ceramics, J. Alloys Compd. 771 (2019) 777–783, https://doi.org/10.1016/j.jallcom.2018.08.259.
[58] D. Chen, Y. Tong, H. Li, J. Wang, Y.L. Zhao, A. Hu, J.J. Kai, Helium accumulation and bubble formation in FeCoNiCr alloy under high fluence He+ implantation, J. Nucl. Mater. 501 (2018) 208–216, https://doi.org/10.1016/J.JNUCMAT.2018.01.041.
[59] K.M. Tynyshbayeva, K.K. Kadyrzhanov, A.L. Kozlovskiy, Y.I. Kuldeyev, V. Uglov, M.V. Zdorovets, Study of helium swelling and embrittlement mechanisms in SiC ceramics, Crystals 12 (2022) 239, https://doi.org/10.3390/cryst12020239.
[60] T. Mościcki, R. Psiuk, D. Jarząbek, M. Ciemiorek-Bartkowska, K. Kulikowski, J. Jasiński, M. Włoczewski, M. Lewandowska, Effect of titanium and deposition parameters on microstructure and mechanical properties of W-Ti-B thin films deposited by High power impulse magnetron sputtering, Surf. Coat. Technol. 485 (2024) 130915, https://doi.org/10.1016/j.surfcoat.2024.130915.
[61] D. Kalita, I. Jóźwik, Ł. Kurpaska, Y. Zhang, K. Mulewska, W. Chrominski, J. O'Connell, Y. Ge, W.L. Boldman, P.D. Rack, Y. Wang, W.J. Weber, J. Jagielski, The microstructure and He+ ion irradiation behavior of novel low-activation W-Ta-Cr-V refractory high entropy alloy for nuclear applications, Nucl. Mater. Energy 37 (2023) 101513, https://doi.org/10.1016/J.NME.2023.101513.
[62] A. Heidarnia, H. Ghomi, Helium ions irradiation of tantalum-zirconium carbide thin films: the effect of acetylene gas contents, Radiat. Phys. Chem. 208 (2023) 110927, https://doi.org/10.1016/J.RADPHYSCHEM.2023.110927.
[63] Z.-M. Yang, K. Zhang, N. Qiu, H.-B. Zhang, Y. Wang, J. Chen, Effects of helium implantation on mechanical properties of (Al0.31Cr0.20Fe0.14Ni0.35)O high entropy oxide films, Chin. Phys. B 28 (2019) 046201, https://doi.org/10.1088/1674-1056/28/4/046201.